EDGE ARTICLE

On-demand photoswitching and energy transfer by post-synthetically confining Eu³⁺-complex and dithienylethene ligand in Zr-MOF-808

Sneha Raj V. Parambil,†[a] Joel Mathew John,†[a] Tarak Nath Das,[b] Adarshi Bhattacharya[a] and Tapas Kumar Maji ID *[ab]

Tailorable porous scaffolds like metal–organic frameworks (MOFs) are emerging as a versatile platform for confining photoresponsive molecules. Herein, we employed a highly stable nanoscale Zr-MOF-808, $\{[Zr_6(\mu_3\text{-}O)_4(\mu_3\text{-}OH)_4(HCOO)_6(BTC)_2]\}_n$ (**Zr-MOF**), as a porous host for post-synthetic incorporation of a carboxylic acid functionalized photochromic dithienylethene (DTE) molecule through the targeted modification of the Zr_6-cluster in the MOF. The post-modified **Zr-DTE-MOF** exhibits a reversible color switching between faint off-white and blue upon UV and visible light irradiation, respectively, owing to the photoisomerization of confined DTE molecules. Furthermore, the nanoscale particle size and excellent dispersibility of **Zr-DTE-MOF** in a suitable solvent enhance its processability as a photochromic ink. Leveraging the prominent spectral overlap between the absorption band of the DTE in closed form and the emission maximum of the Eu³⁺-based complex, we subsequently encapsulated a Eu³⁺–terpyridine-based complex within the MOF pore and constructed a pore-confined photoresponsive donor–acceptor system, named **Zr-DTE-CTPY-Eu-MOF**. The rational selection of suitable donor–acceptor systems for confinement and their close proximity result in fast emission quenching by the photochromic Förster resonance energy transfer (pcFRET) with an appreciable efficiency of 69.9%. Parallely, the **Zr-DTE-CTPY-Eu-MOF** exhibited a photoluminescence quantum yield of 40% (in the open form), which decreased to 14% (in the closed form) after UV light illumination due to the feasible energy transfer from the Eu³⁺–CTPY complex to DTE. Based on the photoswitching ability of the developed photochromic **Zr-DTE-CTPY-Eu-MOF**, it was further employed to create patterns using photomasks, secret writing, and encryption–decryption of confidential information.

ªMolecular Materials Laboratory, Chemistry and Physics of Materials Unit, School of Advanced Materials (SAMat), Jawaharlal Nehru Centre for Advanced Scientific Research (JNCASR), Jakkur, Bangalore 560064, India. E-mail: tmaji@jncasr.ac.in

ᵇNew Chemistry Unit, School of Advanced Materials (SAMat), Jawaharlal Nehru Centre for Advanced Scientifc Research (JNCASR), Jakkur, Bangalore 560064, India

† These authors contributed equally.

Introduction

Materials that exhibit reversible photochromism and modulation of emission properties play a vital role in several applications, including fluorescence microscopy, optical data storage, and sensing.[1–7] The integration of the different photochromic molecules such as spiropyrans, diarylethenes, chromenes, and fulgides, as building blocks in porous scaffolds like metal–organic frameworks (MOF), covalent organic frameworks, and metal–organic cages, has been demonstrated.[8–11] Such photochromic materials are well-explored for different applications including optical switches, optoelectronic devices, sensing, molecular machines, and imaging.[5,6,12–17] Confining photochromic molecules in porous scaffolds can be considered as

a potential strategy for tuning their overall photophysical properties.[1,18,19] In addition, porous scaffolds can overcome the geometric limitations of photoswitching which are typically observed in other solid-state matrices, and improve the photo-fatigue resistance, durability, and mechanical stiffness.[1,18,20] We envisioned that a well-ordered porous framework could provide a suitable platform to uniformly organize photochromic molecules post-synthetically in its nanospace which is not possible in other non-periodic solid matrices.[21,22] Moreover, post-synthetic covalent confinement can ensure the uniform distribution of photochromic molecules along with reduced aggregation and minimized leaching.[18] Also, the porous framework can offer an ideal host for engineering the photochromic Förster resonance energy transfer (pcFRET) process by the confinement of suitable chromophoric acceptor molecules in close proximity to the donor, provided by coordination nanospaces.[23] Such post-synthetic modification of the host MOF can provide precise control over the alignment of suitable donor and acceptor chromophores, allowing flexibility in distance and angle, which would help in realizing the efficient energy transfer process.[24] Such systems would have potential applications in

catalysis, solar cells, sensing, creating patterns using photo-masks, and transferring confidential information.[25–33] A library of photochromic molecules has been studied to understand their feasibility in optoelectronic applications while investigation of their photophysical properties under confinement will be intriguing in the field of optoelectronics.[6,34] The highly promising thermal stability and fatigue-resistant properties of photochromic dithienylethene molecules accompanied by the reversible photoisomerization behaviors expanded their application in optical memory systems, encryption–decryption, molecular switches, and anticounterfeiting devices.[7,35–37] Furthermore, luminescent lanthanide complexes are well known for their emission properties, which include high excited state lifetime, narrow emission bandwidth, and poor photo-bleaching.[38,39] The integration of a photochromic di-thienylethene molecule with luminescent lanthanide complexes in a suitable MOF material by post-synthetic modi-fication can result in the formation of an efficient donor–acceptor system with tunable emission properties and can broaden the understanding of energy transfer in the pcFRET process.[40–42]

In our study, we have chosen Zr-MOF-808, $\{[Zr_6(\mu_3\text{-}O)_4(\mu_3\text{-}OH)_4(HCOO)_6(BTC)_2]\}_n$ (**Zr-MOF**) (BTC: benzene-1,3,5-tri-carboxylate), as a porous host for post-synthetic covalent modification (Fig. 1). The rationale behind choosing the **Zr-MOF** as a host is its stable crystalline porous nature with six post-synthetically exchangeable formate groups at the

secondary building unit (SBU), its nanoscale size in the range of 50–150 nm and non-emissive nature.[26,43] Most importantly, its appropriate pore size allows the coordinative immobilization of desirable chromophoric molecules in a compact way, while the high energy LUMO levels of Zr^{4+} nodes prevent the SBU-involving fluorescence quenching of the chromophoric mole-cule.[44] Additionally, the nanosize of the MOF can enhance its processability by forming a stable dispersion in different solvents. Photochromic **Zr-MOF** has been synthesized by cova-lently integrating the carboxylic acid functionalized photo-switchable dithienylethene-based molecule 4,4′-(perfluorocyclopent-1-ene-1,2-diyl)bis(5-methylthiophene-2-carboxylic acid) (DTE) into the MOF nanopore (Scheme S1 and Fig. S1–4). This nanoscale **Zr-DTE-MOF** with pore-confined DTE molecules exhibited photochromism from faint off-white to blue color upon UV light irradiation, which reversed upon visible light irradiation. We have also investigated the energy transfer between the encapsulated photochromic molecule and a luminescent lanthanide complex under the confinement effect of the MOF pore. For this, **Zr-DTE-MOF** has been modified with π-chromophoric terpyridine-based molecule 4′-(4-carbox-yphenyl)-2,2′:6′,2″-terpyridine (CTPY) (Scheme S2 and Fig. S5) with high triplet state energy via post-synthetic covalent grafting inside the MOF nanopore.[25] The grafted CTPY ligands were further coordinated with Eu^{3+} by post-synthetic metalation, resulting in the red luminescent **Zr-DTE-CTPY-Eu-MOF**. The effective spectral overlap between the absorption maximum of
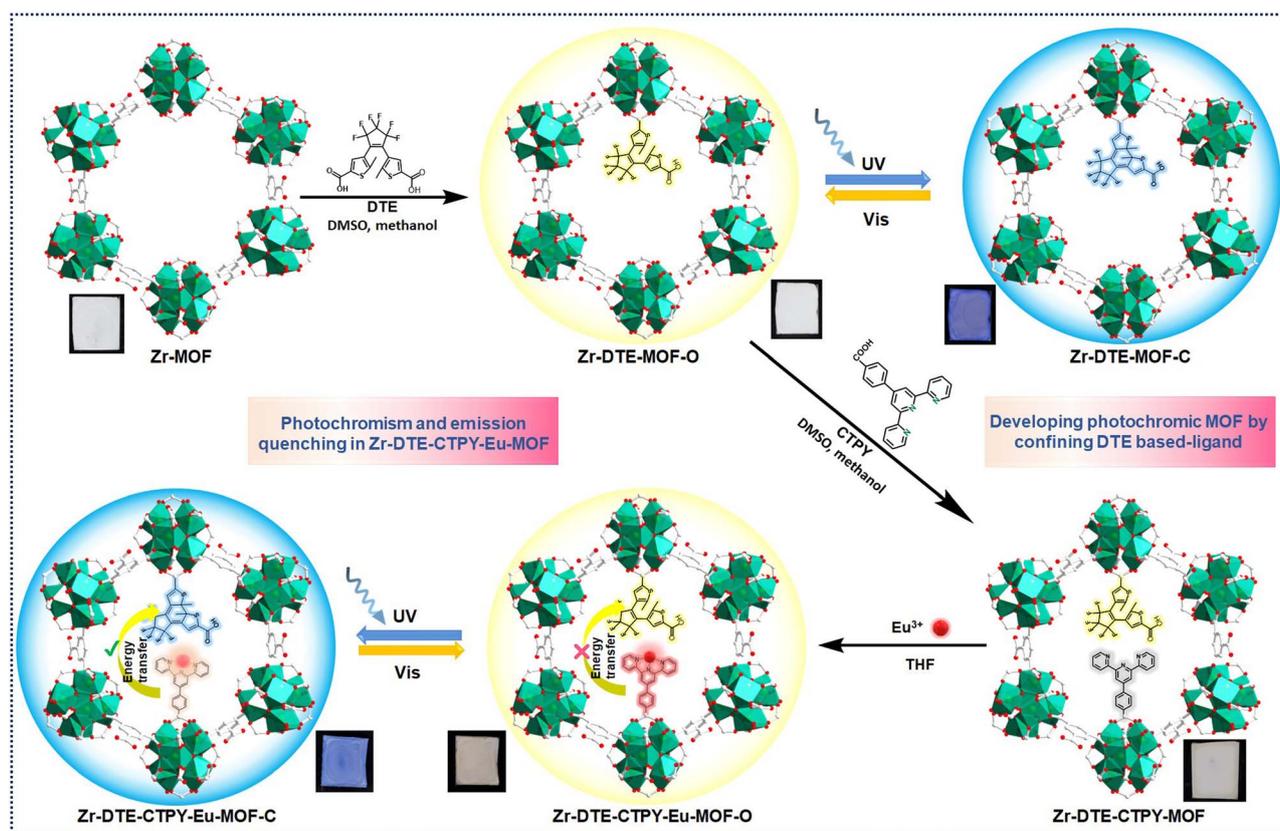

Fig. 1 Schematic representation of post-synthetic modification of **Zr-MOF** for developing photochromic MOFs, illustrating photochromism in **Zr-DTE-MOF** and photochromism and emission quenching in **Zr-DTE-CTPY-Eu-MOF**.

the DTE molecule (in its closed form) and the emission maximum of the Eu^{3+}–CTPY complex facilitated the quenching of lanthanide emission *via* a pcFRET.[45,46] Several molecular systems consisting of lanthanide-based complexes as donors and DTE-based molecules as acceptors have been previously investigated to understand the energy transfer phenomena in the solution state.[45–49] In this study, we have heterogenized such a molecular system by confining it in the MOF pore and explored its photophysical traits. The covalent integration of donor and acceptor molecules within the MOF nanopore facilitated an appreciable energy transfer efficiency of 69.9%, and it demonstrated a highly reversible and kinetically fast solid-state photoswitching from the DTE open form to closed form and *vice versa*. Simultaneously, **Zr-DTE-CTPY-Eu-MOF** depicted a photoluminescence quantum yield of 40% (DTE in the open form), which decreased to 14% (DTE in the closed form) after UV light illumination due to the viable energy transfer from the pore-integrated Eu^{3+}–CTPY complex to DTE in the closed form. Furthermore, the developed photochromic MOFs exhibited excellent liquid state processability and were used as high-precision ink for creating patterns using photomasks, secret writing, and encryption–decryption applications, including confidential information transfer.

Results and discussion

Synthesis and characterization

A highly crystalline nanoscale **Zr-MOF** has been synthesized by the solvothermal method.[43] Formation of **Zr-MOF** was confirmed by the powder X-ray diffraction (PXRD) pattern,

which matches with the simulated pattern obtained from the single crystal dataset (Fig. 2a).[50] The Fourier transform infrared (FTIR) spectrum of **Zr-MOF** showed a peak at 1651 cm^{-1}, which can be ascribed to the coordinated carboxylate group in **Zr-MOF** (Fig. 2b).[51] The N_2 adsorption isotherm analysis at 77 K showed a Brunauer–Emmett–Teller (BET) surface area of 2218 m^2 g^{-1} (Fig. 2c). Additionally, pore size distribution analysis by using nonlocal density functional theory (NLDFT) revealed the presence of pores having a diameter of 1.6 nm (Fig. 2d). Octahedral morphology with particle size ranging from 50–150 nm of the **Zr-MOF** was observed by field emission scanning electron microscopy (FESEM) and high-resolution transmission electron microscopy (HRTEM) imaging (Fig. 2e–g). HRTEM images showed an interplanar distance of 1.6 nm, which is in agreement with the pore size of the MOF (Fig. 2g). ^{1}H-NMR analysis of **Zr-MOF** digested in KOH/D_2O showed the peaks corresponding to six formates and two BTC linkers in the framework, which is in accordance with the framework formula unit $\{[Zr_6(\mu_3\text{-O})_4(\mu_3\text{-OH})_4(HCOO)_6(BTC)_2]\}_n$ (Fig. S6).[50]

A solvent-assisted post-synthetic ligand exchange strategy has been adopted to functionalize the framework with the DTE photochromic molecule.[27,52] The formate group in the SBU has been exchanged with the carboxylate group of the DTE molecule to obtain **Zr-DTE-MOF**. ^{1}H-NMR analysis of digested **Zr-DTE-MOF** showed the reduction of two formate groups in the framework, which in turn implies the covalent integration of two DTE molecules into the Zr_6-cluster of pristine MOF (Fig. S7).[52] Hence the formula unit can be interpreted as $\{[Zr_6(\mu_3\text{-O})_4(\mu_3\text{-OH})_4(HCOO)_4(BTC)(DTE)_2]\}_n$. The PXRD pattern depicted the intactness of crystallinity after the post-
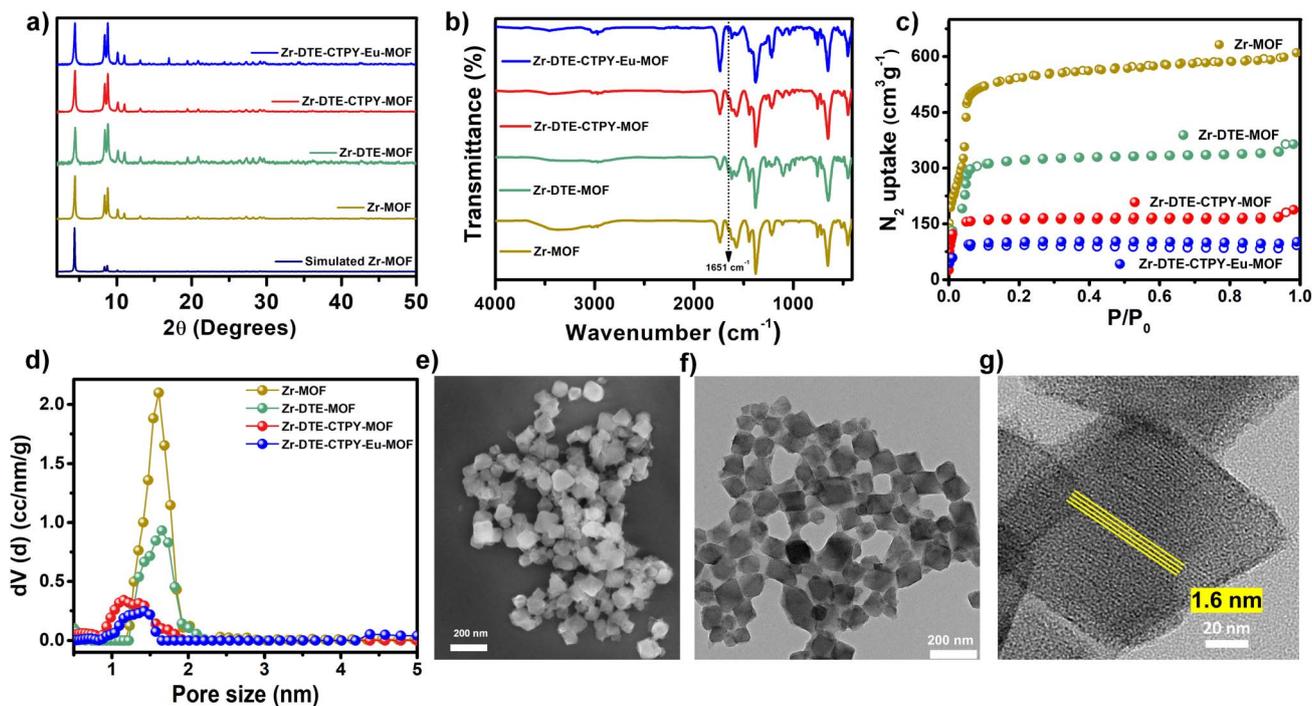

Fig. 2 Different characterizations for **Zr-MOF**, **Zr-DTE-MOF**, **Zr-DTE-CTPY-MOF**, and **Zr-DTE-CTPY-Eu-MOF**: (a) comparison of PXRD patterns. (b) FTIR spectra. (c) N_2 adsorption isotherms at 77 K. (d) Pore size distribution based on the NLDFT method. (e) FESEM image of **Zr-MOF**. (f) TEM image of **Zr-MOF**, (g) HRTEM image of **Zr-MOF** with the lattice fringes.

modifications with DTE as it retained all the peaks of the as-synthesized MOF (Fig. 2a). In addition, covalent encapsulation of DTE in the MOF pore has been confirmed by the N_2 adsorption isotherm, which showed a significant reduction in BET surface area (from 2218 m^2 g^{-1} to 1268 m^2 g^{-1}) and a decreased pore size in comparison to **Zr-MOF** (Fig. 2c and d). The as-synthesized **Zr-DTE-MOF** exhibited a faint off-white color, in which DTE molecules are in a ring-opened form, and the MOF in which DTE is in its open form is abbreviated as **Zr-DTE-MOF-O.** Upon irradiation of UV light (λ < 400 nm, center wavelength = 325 nm), **Zr-DTE-MOF-O** turns blue with a gradual increase in the absorption maxima around 583 nm attributed to the ring closing of the DTE molecule (Fig. 3a).[53] **Zr-DTE-MOF** with DTE in its closed form is abbreviated as **Zr-DTE-MOF-C.** The kinetics plot obtained from UV-visible spectra showed that this conversion is saturated after 40 seconds (Fig. 3a). The MOF-confined photocyclization of the DTE molecule is completely reversible, and it can be easily reversed by visible light

irradiation (λ > 400 nm). The diffuse reflectance UV-visible spectra of **Zr-DTE-MOF-C** showed a gradual decrease in the peak around 500–600 nm upon visible light irradiation, corresponding to the conversion of the DTE molecule from its closed form to the open form and attained saturation after 30 seconds (Fig. 3b and c).[54,55] However, the saturation time entirely depends on factors including the power and wavelength of the light source applied, and the distance between the sample and the light source. Fig. 3d depicts the reverse photochromism exhibited by **Zr-DTE-MOF** in the solid as well as dispersion state (in acetonitrile) from faint off-white to blue and *vice versa*. The estimated quantum yield for the photoisomerization of MOF-confined DTE, from **Zr-DTE-MOF-C** to **Zr-DTE-MOF-O**, with 550 nm light illumination is 62%.[56,57]

Next, we have covalently encapsulated the CTPY by exchanging the formate linkage with the carboxylate group of CTPY molecules, forming **Zr-DTE-CTPY-MOF**.[25] The ^{1}H-NMR spectrum of digested **Zr-DTE-CTPY-MOF** showed a further
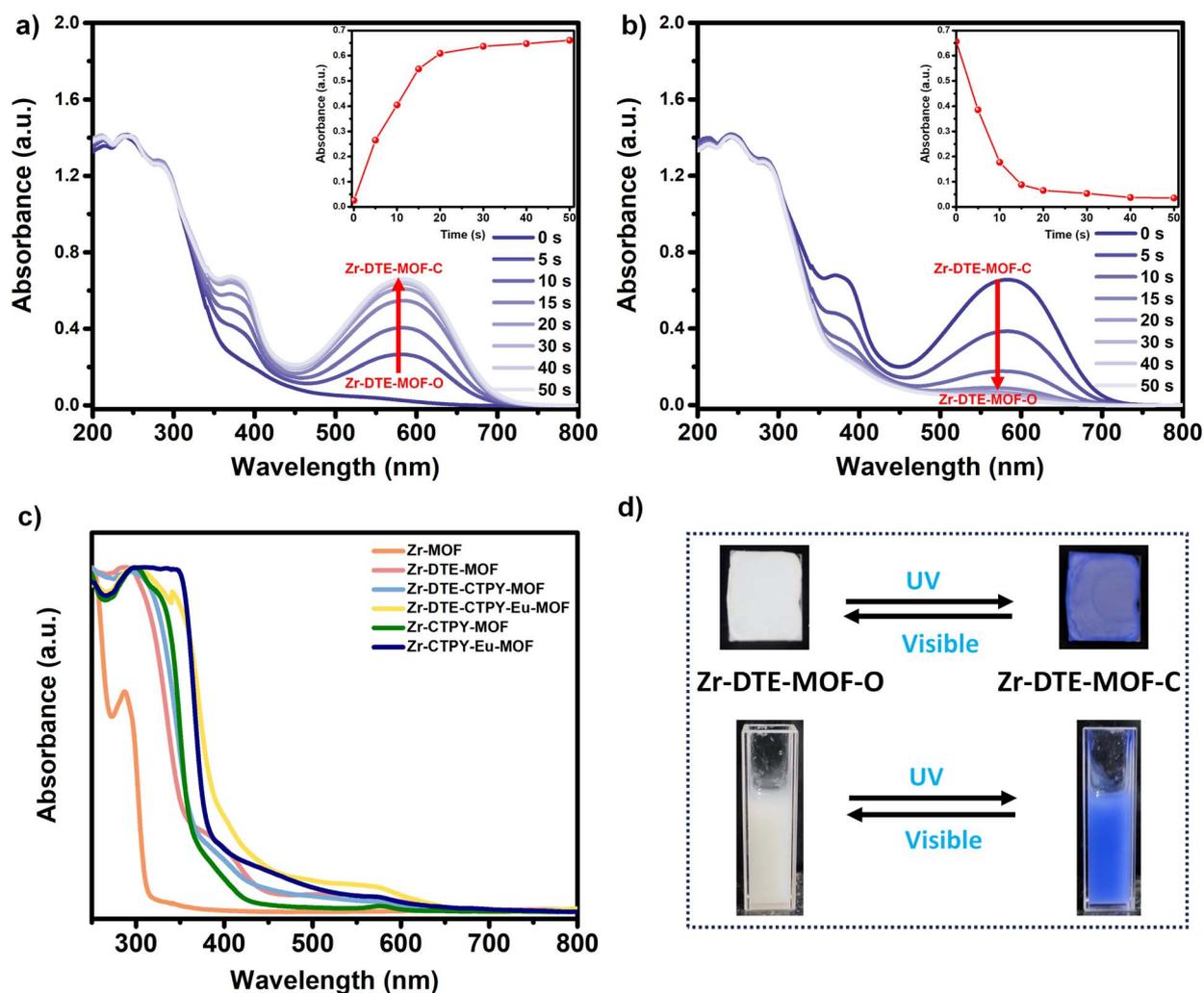

Fig. 3 Time-dependent changes in diffuse reflectance UV-Vis spectra of **Zr-DTE-MOF** (a) upon irradiation of UV light (inset shows the kinetics of absorption spectra at 583 nm) and (b) upon irradiation of visible light (inset shows the kinetics of absorption spectra at 583 nm). (c) Diffuse reflectance UV-visible spectra of **Zr-MOF**, **Zr-DTE-MOF**, **Zr-DTE-CTPY-MOF**, **Zr-DTE-CTPY-Eu-MOF**, **Zr-CTPY-MOF**, and **Zr-CTPY-Eu-MOF**, (d) photographs showing the reversible photochromism exhibited by **Zr-DTE-MOF** in solid and dispersion states (dispersed in acetonitrile) upon UV and visible light irradiation.

decrease of one formate molecule (Fig. S8). Correspondingly, the BET surface area was reduced to 623 m^2 g^{-1} in **Zr-DTE-CTPY-MOF** in comparison to **Zr-DTE-MOF**, which could imply the coordination of one CTPY in the SBU (Fig. 2c). Moreover, the pore volume was also reduced significantly, which further ensures the CTPY encapsulation inside the MOF pore (Fig. 2d). Following the covalent grafting of CTPY inside the MOF, **Zr-DTE-CTPY-MOF** has been reacted with Eu(NO$_3$)$_3$·6H$_2$O. Terpyridine nitrogens can act as potential sites for the coordination of Eu^{3+}.[25,58] Hence, three coordination sites of Eu^{3+} are occupied by three N from CTPY units with 1 : 1 CTPY : Eu^{3+} coordination, and the remaining coordination sites can be satisfied by H$_2$O and bidentate nitrate groups as previously reported.[25,59,60] The 2 : 1 ratio of CTPY to Eu^{3+} can be ruled out due to the size constraints, as shown in our previous study.[25] Therefore, the confined Eu^{3+}–CTPY complex in the nanospace of the MOF pore resulted in the formation of luminescent red light-emitting MOF, named **Zr-DTE-CTPY-Eu-MOF**. The PXRD pattern and the morphology of the **Zr-DTE-CTPY-Eu-MOF** remain intact, as shown in Fig. 2a and S9. The BET surface area of **Zr-DTE-CTPY-Eu-MOF** was further decreased to 364 m^2 g^{-1} (Fig. 2c). The slight reduction in the surface area and pore size can also support the coordination of Eu^{3+} with CTPY (Fig. 2d). From the UV-visible spectrum, **Zr-MOF** displayed absorbance in the region of 280 nm, which corresponds to the π to π* transitions of the BTC linker (Fig. 3c).[52] Meanwhile, the absorption band extending up to 330 nm in the UV-Vis spectrum of **Zr-DTE-CTPY-Eu-MOF** can be assigned to the π to π* transitions associated with the CTPY ligands (Fig. 3c).[25,61] Further, inductively coupled plasma-optical emission spectroscopy (ICP-OES) analysis has been performed

to quantify Eu in the framework. The digested **Zr-DTE-CTPY-Eu-MOF** showed Eu loading of 1.1 per Zr$_6$ SBU corresponding to a Zr : Eu ratio of 6 : 1.1, thereby implying the presence of approximately one Eu per formula unit. The distribution of Zr, O, N, Eu, S, F, and C throughout the nanocrystal has been observed from the energy-dispersive X-ray (EDX) elemental mapping analysis, which supports uniform incorporation of DTE molecules and the Eu^{3+}–CTPY complex in the framework (Fig. S10a–c). Further high-resolution X-ray photoelectron spectroscopy (XPS) analysis also indicated the presence of Zr, Eu, N, F, O, S, and C (Fig. S11a–g). The high-resolution XPS spectrum of Zr displayed two peaks at 182.7 and 185.15 eV, corresponding to Zr^{4+} 3d$_{5/2}$ and 3d$_{3/2}$, respectively (Fig. S11a).[62] Similarly, the peaks at 1135.5 and 1165 eV can be assigned to Eu^{3+} 3d$_{5/2}$ and 3d$_{3/2}$, respectively (Fig. S11b).[63,64] Moreover, N 1s analysis revealed the presence of coordinated pyridinic N at 400.5 eV (Fig. S11c).[64] Additionally, F 1s peak is also observed at 688 eV, attributed to the C–F bonds in the DTE molecule (Fig. S11d).[65] S 2p analysis depicted 2p$_{3/2}$ and 2p$_{1/2}$ at 164.3 and 165.6 eV, respectively, which arises due to the presence of DTE molecules inside the MOF (Fig. S11f).[66] C 1s XPS spectra can be deconvoluted into 5 distinct peaks positioned at 284.9, 285.8, 286.8, 288.7, and 290.6 eV corresponding to the presence of C–C, C–S, C–N, C–O, and C–F bonds (Fig. S11g).[27,66,67] Cumulative analysis of the above-mentioned characterizations concludes the successful covalent integration of DTE molecule and the Eu^{3+}–CTPY complex in the confined space of the MOF nanopore.

After the detailed characterization of the material, we performed photoisomerization and photochromic energy transfer
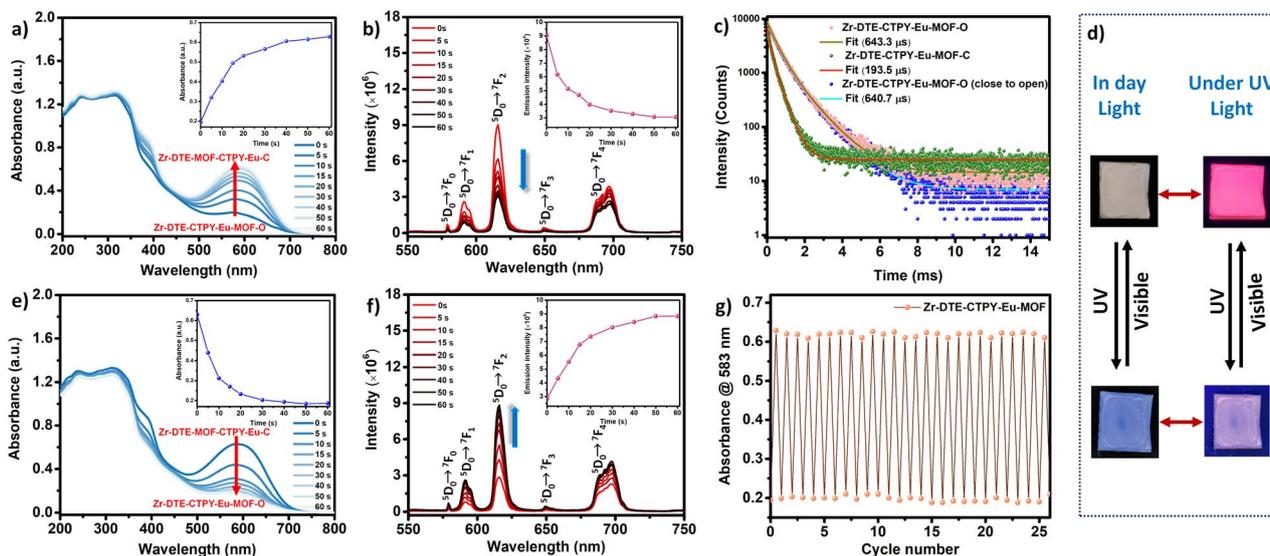

Fig. 4 Time-dependent changes in (a) diffuse reflectance UV-Vis spectra of **Zr-DTE-CTPY-Eu-MOF** upon irradiation of UV light (inset shows the kinetics of absorption spectra at 583 nm), (b) emission spectra of **Zr-DTE-CTPY-Eu-MOF** upon irradiation of UV light (λ_{ex} = 330 nm) (inset shows the kinetics of emission spectra at 616 nm), (c) lifetime decay profile of **Zr-DTE-CTPY-Eu-MOF-O**, **Zr-DTE-CTPY-Eu-MOF-C**, and **Zr-DTE-CTPY-Eu-MOF-O** (closed to open form) (λ_{ex} = 290 nm, $\lambda_{collected}$ = 616 nm), (d) photographs showing the reversible photochromism and emission quenching exhibited by **Zr-DTE-CTPY-Eu-MOF** upon UV and visible light irradiation, (e) diffuse reflectance UV-Vis spectra of **Zr-DTE-CTPY-Eu-MOF** upon irradiation of visible light (inset shows the kinetics of absorption spectra at 583 nm) and (f) emission spectra of **Zr-DTE-CTPY-Eu-MOF** upon irradiation of visible light (λ_{ex} = 330 nm) (inset shows the kinetics of emission spectra at 616 nm), (g) change in the absorption intensity of **Zr-DTE-CTPY-Eu-MOF** upon UV and visible light irradiation over 25 cycles.

studies. Similar to **Zr-DTE-MOF**, the diffuse reflectance UV-Vis spectrum of **Zr-DTE-CTPY-Eu-MOF** showed a gradual increase in the peak centered at around 500–600 nm upon UV light irradiation by the photocyclization of the DTE molecule from its open form to its closed form (Fig. 4a). The band formed upon light irradiation indicates ring closing of the DTE molecule confined in the MOF pore. The kinetics plot indicates the maximum conversion was achieved after 40 seconds of UV light irradiation, similar to **Zr-DTE-MOF** (Fig. 4a). Parallelly, emission spectra were also collected to understand the emission quenching of the Eu^{3+}–CTPY complex (Fig. 4b). Before the irradiation of UV light, the intense red emission consists of peaks appearing at 579 ($^5D_0 \rightarrow {}^7F_0$), 591 ($^5D_0 \rightarrow {}^7F_1$), 616 ($^5D_0 \rightarrow {}^7F_2$), 649 ($^5D_0 \rightarrow {}^7F_3$), and 693 ($^5D_0 \rightarrow {}^7F_4$) is observed, which are attributed to the presence of Eu^{3+}–CTPY complex inside the MOF.[25,55] Additionally, we have also synthesized **Zr-CTPY-Eu-MOF** for controlled study, without having confined DTE molecules, and it was characterized by ^{1}H-NMR, PXRD, FTIR, and UV-visible absorption spectroscopy (Fig. S12–15 and 3c). It showed an emission spectrum similar to that of **Zr-DTE-CTPY-Eu-MOF** with an average photoluminescence lifetime of 666.2 μs (Fig. S16 and 17). The possibility of ligand-sensitized emission with CTPY has been shown in our previous work by calculating the triplet excited state energy of the CTPY ligand using time-dependent density functional theory.[25] This can also confirm the coordination of Eu^{3+} with CTPY, resulting in an intense red emission. However, we have also treated the **Zr-DTE-MOF** with $Eu(NO_3)_3 \cdot 6H_2O$ by following a similar procedure used for **Zr-CTPY-Eu-MOF** synthesis. The resulting material does not exhibit red emission, thereby confirming that Eu^{3+} prefers to coordinate with the CTPY ligand inside the pore rather than the free carboxylate group of the DTE molecule (Fig. S18). The emission intensity of the Eu^{3+}–CTPY complex in **Zr-DTE-CTPY-Eu-MOF** diminished with time of UV light irradiation (Fig. 4b).[54] The effective overlap of the emission spectrum of the Eu^{3+}–CTPY complex with the absorbance of the DTE molecule in its closed form, and the minimum distance

between these MOF-confined donor–acceptor molecules resulted in effective energy transfer from the Eu^{3+}–CTPY complex to the DTE molecule (Fig. S19), thereby significantly reducing the lanthanide emission intensity. In addition, a prominent change in the average lifetime is also observed before and after UV light irradiation. **Zr-DTE-CTPY-Eu-MOF-O** (where the DTE is in its open form) showed an average lifetime of 643.3 μs, whereas upon UV-light irradiation its average lifetime decreased to 193.5 μs, further corroborating the energy transfer process by the ring-closing of DTE in MOF to form **Zr-DTE-CTPY-Eu-MOF-C** (Fig. 4c). The lifetime reduction of the Eu^{3+}–CTPY complex in the presence of the DTE molecule inside the MOF pore indicated the energy transfer process with an efficiency of 69.9%. Fig. 4d depicts the reversible photochromism from yellowish off-white to blue and corresponding changes in the emission intensity of **Zr-DTE-CTPY-Eu-MOF** under ambient and UV light. Moreover, the photoluminescent quantum yield of the Eu^{3+}–CTPY complex inside **Zr-DTE-CTPY-Eu-MOF** was measured to be 40%, which reduced to 14% after UV light irradiation. This reduction is attributed to the ring-closing of **DTE** molecules, which resulted the energy transfer from Eu^{3+}–CTPY complex to DTE. Additionally, the physical mixture of **Zr-CTPY-Eu-MOF** and **Zr-DTE-MOF** has been prepared, and its excited state lifetime was 630.8 μs, whereas the lifetime upon UV light irradiation was slightly reduced to 598.1 μs (Fig. S20). From this, the energy transfer efficiency is calculated to be ~5%, which is remarkably lower than that of **Zr-DTE-CTPY-Eu-MOF**, where both the donor and acceptor are at a favorable distance for energy transfer. This validates the importance of the confinement of the acceptor DTE and donor Eu^{3+}–CTPY complex in close proximity inside the MOF pore for an efficient energy transfer process.

The photocyclization process in **Zr-DTE-CTPY-Eu-MOF** is completely reversible with irradiation of visible light of wavelength >400 nm. Upon irradiation, the diffuse reflectance UV-Vis spectrum of **Zr-DTE-CTPY-Eu-MOF** (with DTE in its closed form) showed a gradual decrease in the absorption intensity in the region of 500–600 nm (Fig. 4e). This decrease indicates the
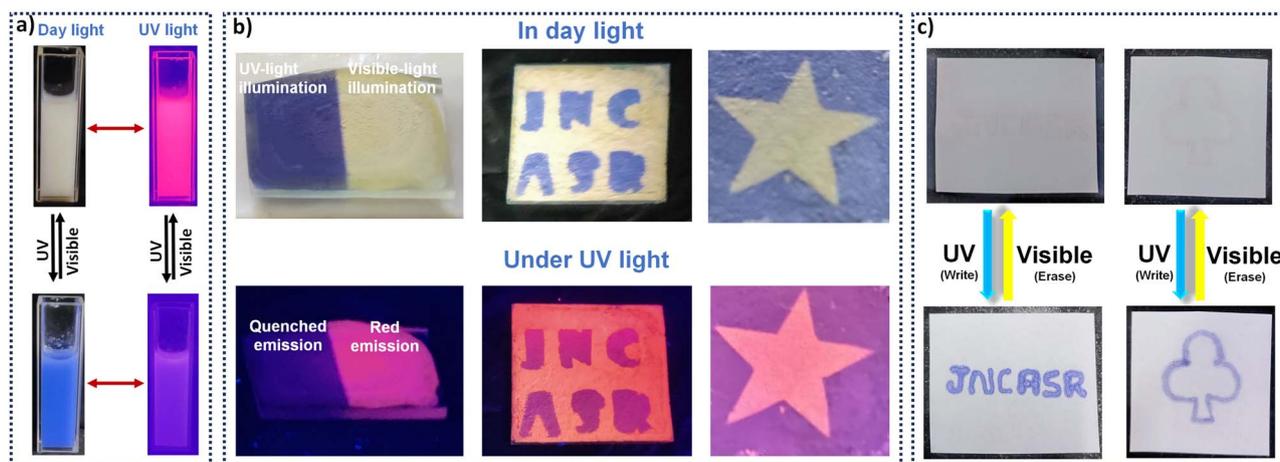

Fig. 5 (a) Photographs showing the reversible photochromism and emission quenching exhibited by **Zr-DTE-CTPY-Eu-MOF** (dispersed in acetonitrile) in daylight and under UV light, (b) various shapes obtained by using photomasks on **Zr-DTE-CTPY-Eu-MOF** in daylight and under UV light, (c) photograph showing the encryption–decryption of information by using **Zr-DTE-MOF** as an ink on ordinary paper.

conversion of confined DTE molecules from closed form to open form. The kinetics plot based on the UV-visible spectra showed the conversion attained saturation after 30 seconds (Fig. 4e). A simultaneous increment in the lanthanide emission intensity is also observed due to the formation of DTE in the open form, which does not possess any absorption overlap with the emission spectrum of the Eu^{3+}–CTPY complex (Fig. 4f). The reversible photochromic nature of **Zr-DTE-CTPY-Eu-MOF** has been probed 25 times by measuring the UV-visible spectra (Fig. 4g). It showed a similar profile to that of the first cycle suggesting the promising fatigue resistance behavior of the developed MOF. In addition, **Zr-DTE-CTPY-Eu-MOF** from its closed form to open form showed an appreciable photo-isomerization quantum yield of about 60% (Fig. S21a and b). The slight decrease in the photoisomerization conversion efficiency of DTE in the presence of the Eu^{3+}–CTPY complex can be attributed to the possible steric hindrance in the system.

Taking advantage of the high stability of **Zr-MOF** and the highly reversible photoswitching ability attained by the encapsulated DTE molecule, **Zr-DTE-MOF** and **Zr-DTE-CTPY-Eu-MOF** are utilised as suitable inks for creating patterns using photomasks, secret writing, and encryption–decryption. Importantly, the synthesized **Zr-DTE-MOF**, **Zr-DTE-CTPY-Eu-MOF**, and **Zr-CTPY-Eu-MOF** depicted excellent liquid state processability by forming a stable dispersion in a suitable solvent (Fig. 3d, 5a and S22a). The high dispersibility of the photochromic MOF can be attributed to its nanoscale particle size, which is helpful in the preparation of ink for creating patterns using photomasks and encryption–decryption applications. Moreover, the photoswitching process is kinetically fast and reversible; hence, the color and emission can be switched by irradiation of light with suitable wavelength. This light-induced photoswitching and emission-quenching property of the **Zr-DTE-CTPY-Eu-MOF** can be useful for creating various patterns and shapes using photomasks, as shown in Fig. 5b and S22b. The fast reading and erasing capability of this photochromic MOF is also demonstrated for secret writing and erasing to transfer confidential information. As shown in Fig. 5c, a message was written on ordinary paper using **Zr-DTE-MOF** ink, which can be easily read out after irradiating UV light and can be erased by visible light. Similarly, photo-printing has also been demonstrated by using **Zr-DTE-CTPY-Eu-MOF** ink. We have investigated the decoding of the QR code to our institute website (Jawaharlal Nehru Centre for Advanced Scientific Research, JNCASR) by using the fluorescent **Zr-DTE-CTPY-Eu-MOF** ink (Fig. 6a, b and SI Movie). The photo-printing has been done by irradiating UV light on the sample through the reverse QR code photomask. The photoprinted QR code on the MOF surface can be decoded easily by scanning under UV light and erased by illuminating with visible light. The decoding of the QR code created on the **Zr-CTPY-DTE-Eu-MOF** proves its potential function as a high-precision ink for encryption–decryption applications. The uniform distribution of DTE and Eu^{3+}–CTPY complex in the confined space of the MOF nanopore minimized the smudging and smearing, ensuring the high readability and durability of this material.
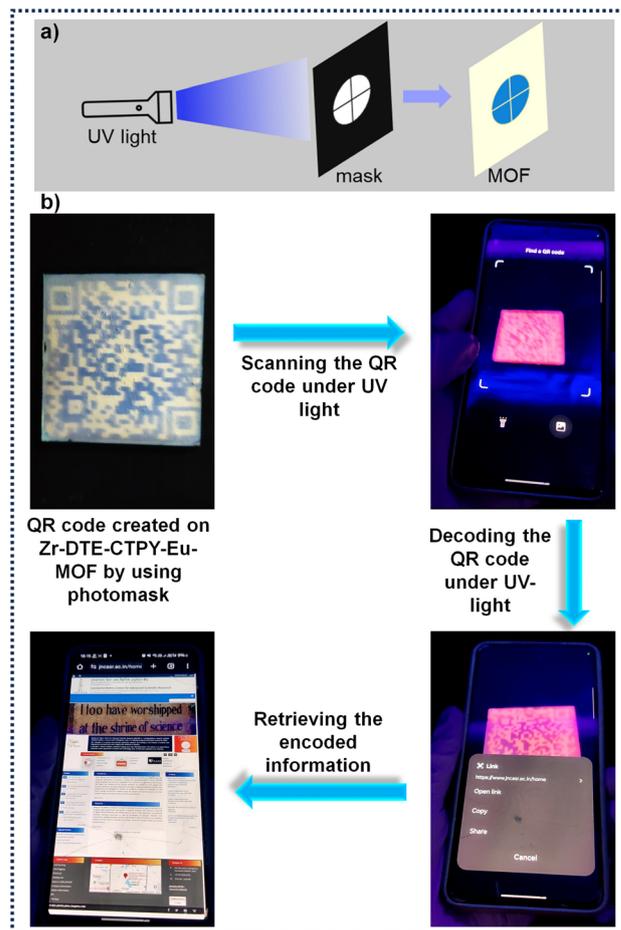

Fig. 6 (a) Schematic representation of information writing using a photomask. (b) Photographs illustrating the scanning of the photo-printed QR code on **Zr-DTE-CTPY-Eu-MOF** with a mobile phone.

Conclusions

In summary, the present study illustrates the heterogenization of photoswitchable DTE molecules in porous scaffolds to enhance their stability and attain high-energy transfer efficiencies by utilizing the confinement effect. We have adopted multi-step post-synthetic modification strategies to covalently encapsulate the dithienylethene-based derivative inside the MOF nanopore and successfully integrated the photochromic behavior into the MOF matrix. The developed photochromic MOFs depicted fast and reversible solid-state photoswitching and energy transfer in the presence of the confined highly emissive Eu^{3+}–terpyridine-based lanthanide complex in close proximity. The custom-designed **Zr-DTE-CTPY-Eu-MOF** exhibited a high energy transfer efficiency of 69.9% when compared to its corresponding solid-state physical mixture. Highly reversible photoswitching has been achieved in the MOF-confined state with an appreciably fast photoisomerization and exhibited more than 25 cycles of photoswitching. Along with that, its liquid state processability by forming a stable dispersion is highly useful for creating patterns using photomasks, secret writing, and encryption–decryption in information transfer.

Finally, this study demonstrates the importance of designing highly stable MOF-confined photochromic systems for enhancing the efficiency of photochromic energy transfer and solid-state photoswitching applications.

Author contributions

Conflicts of interest

There are no conflicts to declare.

Data availability

Additional figures and tables are provided in the SI. Supplementary information: Synthetic procedure, experimental details, ^{1}H-NMR spectra, FESEM images, EDX analysis, XPS spectra, UV-visible absorbtion spectra, PXRD patterns, emission spectrum, lifetime decay profile, energy transfer efficiency calculations, and photoisomerization quantum yield calculations. See DOI: https://doi.org/10.1039/d5sc06243h.

Acknowledgements

Notes and references

1 G. A. Leith, C. R. Martin, J. M. Mayers, P. Kittikhunnatham, R. W. Larsen and N. B. Shustova, *Chem. Soc. Rev.*, 2021, **50**, 4382–4410.

2 T. Wu, X.-j. Gao, F. Ge and H.-g. Zheng, *CrystEngComm*, 2022, **24**, 7881–7901.

3 J. Cusido, E. Deniz and F. M. Raymo, *Curr. Phys. Chem.*, 2011, **1**, 232–241.

4 S. Kawata and Y. Kawata, *Chem. Rev.*, 2000, **100**, 1777–1788.

5 M. Qin, Y. Huang, F. Li and Y. Song, *J. Mater. Chem. C*, 2015, **3**, 9265–9275.

6 J. Zhang, Q. Zou and H. Tian, *Adv. Mater.*, 2013, **25**, 378–399.

7 J. Guo, Y. Gao, M. Pan, X. Li, F. Kong, M. Wu, L. Zhang, Z. Cheng, R. Zhao and H. Ma, *ACS Appl. Mater. Interfaces*, 2024, **16**, 23703–23716.

8 D. E. Williams, J. A. Rietman, J. M. Maier, R. Tan, A. B. Greytak, M. D. Smith, J. A. Krause and N. B. Shustova, *J. Am. Chem. Soc.*, 2014, **136**, 11886–11889.

9 Y. Zheng, H. Sato, P. Wu, H. J. Jeon, R. Matsuda and S. Kitagawa, *Nat. Commun.*, 2017, **8**, 100.

10 A. M. Rice, C. R. Martin, V. A. Galitskiy, A. A. Berseneva, G. A. Leith and N. B. Shustova, *Chem. Rev.*, 2019, **120**, 8790–8813.

11 A. B. Grommet, L. M. Lee and R. Klajn, *Acc. Chem. Res.*, 2020, **53**, 2600–2610.

12 M. Irie, *Chem. Rev.*, 2000, **100**, 1683–1684.

13 H. Tian and Y. Feng, *J. Mater. Chem.*, 2008, **18**, 1617–1622.

14 Y. Ru, Z. Shi, J. Zhang, J. Wang, B. Chen, R. Huang, G. Liu and T. Yu, *Mater. Chem. Front.*, 2021, **5**, 7737–7758.

15 M. Irie, *Bull. Chem. Soc. Jpn.*, 2008, **81**, 917–926.

16 S. Corra, M. Curcio, M. Baroncini, S. Silvi and A. Credi, *Adv. Mater.*, 2020, **32**, 1906064.

17 J. Zhang, J. Wang and H. Tian, *Mater. Horiz.*, 2014, **1**, 169–184.

18 S. Mollick and J.-C. Tan, *Nat. Rev. Mater.*, 2025, **10**, 519–535.

19 A. B. Grommet, M. Feller and R. Klajn, *Nat. Nanotechnol.*, 2020, **15**, 256–271.

20 D. E. Williams, C. R. Martin, E. A. Dolgopolova, A. Swifton, D. C. Godfrey, O. A. Ejegbavwo, P. J. Pellechia, M. D. Smith and N. B. Shustova, *J. Am. Chem. Soc.*, 2018, **140**, 7611–7622.

21 H. Furukawa, K. E. Cordova, M. O'Keeffe and O. M. Yaghi, *Science*, 2013, **341**, 1230444.

22 G. C. Thaggard, B. K. M. Kankanamalage, K. C. Park, J. Lim, M. A. Quetel, M. Naik and N. B. Shustova, *Adv. Mater.*, 2024, 2410067.

23 D. Hermann, H. Emerich, R. Lepski, D. Schaniel and U. Ruschewitz, *Inorg. Chem.*, 2013, **52**, 2744–2749.

24 W. Cao, Y. Tang, Y. Cui and G. Qian, *Small Struct.*, 2020, **1**, 2000019.

25 S. Karmakar, A. Ghosh, F. A. Rahimi, B. Rawat and T. K. Maji, *ACS Appl. Mater. Interfaces*, 2022, **14**, 49014–49025.

26 S. R. V. Parambil, S. Karmakar, F. A. Rahimi and T. K. Maji, *ACS Appl. Mater. Interfaces*, 2023, **15**, 27821–27831.

27 S. R. V. Parambil, F. A. Rahimi, R. Ghosh, S. Nath and T. K. Maji, *Inorg. Chem.*, 2023, **62**, 19312–19322.

28 N. K. Kulachenkov, D. Sun, Y. A. Mezenov, A. N. Yankin, S. Rzhevskiy, V. Dyachuk, A. Nominé, G. Medjahdi, E. A. Pidko and V. A. Milichko, *Angew. Chem., Int. Ed.*, 2020, **59**, 15522–15526.

29 H.-Y. Li, Y.-L. Wei, X.-Y. Dong, S.-Q. Zang and T. C. Mak, *Chem. Mater.*, 2015, **27**, 1327–1331.

30 G. C. Thaggard, J. Haimerl, K. C. Park, J. Lim, R. A. Fischer, B. K. Maldeni Kankanamalage, B. J. Yarbrough, G. R. Wilson and N. B. Shustova, *J. Am. Chem. Soc.*, 2022, **144**, 23249–23263.

31 R. Samanta, D. Kitagawa, A. Mondal, M. Bhattacharya, M. Annadhasan, S. Mondal, R. Chandrasekar, S. Kobatake and C. M. Reddy, *ACS Appl. Mater. Interfaces*, 2020, **12**, 16856–16863.

32 Y.-P. Song, J.-N. Zhang, J.-R. Wang, K. Li, Y.-X. Yuan, B. Li and S.-Q. Zang, *Sci. China Mater.*, 2024, **67**, 698–704.

33 R. Jena, F. A. Rahimi, S. Karmakar, A. Dey, D. Kalita, T. N. Das and T. K. Maji, *Adv. Funct. Mater.*, 2024, **34**, 2407721.

34 S. Chatterjee, S. Molla, J. Ahmed and S. Bandyopadhyay, *Chem. Commun.*, 2023, **59**, 12685–12698.

35 J. C.-H. Chan, W. H. Lam and V. W.-W. Yam, *J. Am. Chem. Soc.*, 2014, **136**, 16994–16997.

36 H. Tian and S. Yang, *Chem. Soc. Rev.*, 2004, **33**, 85–97.

37 S. Jana, S. K. Bag, B. Mondal, M. Karmakar and A. Thakur, *Organometallics*, 2024, **43**, 1459–1471.

38 H. Dong, L.-D. Sun and C.-H. Yan, *Nanoscale*, 2013, **5**, 5703–5714.

39 S. Karmakar, A. Ghosh, K. Prasad, F. A. Rahimi, D. Rambabu, R. Haldar and T. K. Maji, *Dalton Trans.*, 2021, **50**, 13002–13011.

40 L. Giordano, T. M. Jovin, M. Irie and E. A. Jares-Erijman, *J. Am. Chem. Soc.*, 2002, **124**, 7481–7489.

41 D. Samanta, A. Singh, P. Verma, S. Bhattacharyya, S. Roy and T. K. Maji, *J. Org. Chem.*, 2019, **84**, 10946–10952.

42 F. Zhao, H. Cai, Z. Song and Q. Liu, *Chem. Mater.*, 2021, **33**, 8360–8366.

43 J. Jiang, F. Gándara, Y.-B. Zhang, K. Na, O. M. Yaghi and W. G. Klemperer, *J. Am. Chem. Soc.*, 2014, **136**, 12844–12847.

44 G. C. Thaggard, G. A. Leith, D. Sosnin, C. R. Martin, K. C. Park, M. K. McBride, J. Lim, B. J. Yarbrough, B. K. Maldeni Kankanamalage and G. R. Wilson, *Angew. Chem., Int. Ed.*, 2023, **62**, e202211776.

45 Z. Li, X. Liu, G. Wang, B. Li, H. Chen, H. Li and Y. Zhao, *Nat. Commun.*, 2021, **12**, 1363.

46 H.-B. Cheng, G.-F. Hu, Z.-H. Zhang, L. Gao, X. Gao and H.-C. Wu, *Inorg. Chem.*, 2016, **55**, 7962–7968.

47 H. Al Sabea, L. Norel, O. Galangau, T. Roisnel, O. Maury, F. Riobé and S. Rigaut, *Adv. Funct. Mater.*, 2020, **30**, 2002943.

48 T. Nakagawa, Y. Hasegawa and T. Kawai, *J. Phys. Chem. A*, 2008, **112**, 5096–5103.

49 F. Hu, X. Li, Y. Leng, Y. Zhang, M. Zhou and Y. Ou, *Inorg. Chim. Acta*, 2017, **458**, 45–49.

50 H. Furukawa, F. Gándara, Y.-B. Zhang, J. Jiang, W. L. Queen, M. R. Hudson and O. M. Yaghi, *J. Am. Chem. Soc.*, 2014, **136**, 4369–4381.

51 A. Singh, S. Karmakar, I. M. Abraham, D. Rambabu, D. Dave, R. Manjithaya and T. K. Maji, *Inorg. Chem.*, 2020, **59**, 8251–8258.

52 S. Karmakar, S. Barman, F. A. Rahimi and T. K. Maji, *Energy Environ. Sci.*, 2021, **14**, 2429–2440.

53 T. Kaieda, S. Kobatake, H. Miyasaka, M. Murakami, N. Iwai, Y. Nagata, A. Itaya and M. Irie, *J. Am. Chem. Soc.*, 2002, **124**, 2015–2024.

54 P. Verma, A. Singh and T. K. Maji, *Chem. Sci.*, 2021, **12**, 2674–2682.

55 Z. Li, H. Chen, B. Li, Y. Xie, X. Gong, X. Liu, H. Li and Y. Zhao, *Adv. Sci.*, 2019, **6**, 1901529.

56 C. R. Martin, K. C. Park, G. A. Leith, J. Yu, A. Mathur, G. R. Wilson, G. B. Gange, E. L. Barth, R. T. Ly, O. M. Manley, K. L. Forrester, S. G. Karakalos, M. D. Smith, T. M. Makris, A. K. Vannucci, D. V. Peryshkov and N. B. Shustova, *J. Am. Chem. Soc.*, 2022, **144**, 4457–4468.

57 K. Stranius and K. Börjesson, *Sci. Rep.*, 2017, **7**, 1–9.

58 O. Kotova, R. Daly, C. M. dos Santos, M. Boese, P. E. Kruger, J. J. Boland and T. Gunnlaugsson, *Angew. Chem., Int. Ed.*, 2012, **51**, 7208–7212.

59 F. D. White, A. N. Gaiser, E. J. Warzecha, J. M. Sperling, C. Celis-Barros, S. R. Salpage, Y. Zhou, T. Dilbeck, A. J. Bretton and D. S. Meeker, *Inorg. Chem.*, 2018, **57**, 12969–12975.

60 A. E. Sedykh, M. Maxeiner, M. T. Seuffert, D. Heuler, D. G. Kurth and K. Müller-Buschbaum, *Eur. J. Inorg. Chem.*, 2024, **27**, e202400078.

61 S. Lee, K. Y. Kim, N. Y. Lim, J. H. Jung, J. H. Lee, M. Y. Choi and J. H. Jung, *J. Hazard. Mater.*, 2019, **378**, 120713.

62 Z.-J. Lin, H.-Q. Zheng, Y.-N. Zeng, Y.-L. Wang, J. Chen, G.-J. Cao, J.-F. Gu and B. Chen, *Chem. Eng. J.*, 2019, **378**, 122196.

63 J.-G. Kang, Y. Jung, B.-K. Min and Y. Sohn, *Appl. Surf. Sci.*, 2014, **314**, 158–165.

64 M. H. Joo, S. J. Park, H. J. Jang, S.-M. Hong, C. K. Rhee and Y. Sohn, *Photochem*, 2021, **1**, 38–52.

65 S. Sarkar, S. Garain, D. Mandal and K. Chattopadhyay, *RSC Adv.*, 2014, **4**, 48220–48227.

66 C. Varodi, F. Pogăcean, A. Cioriță, O. Pană, C. Leoștean, B. Cozar, T. Radu, M. Coroș, R. I. Ștefan-van Staden and S.-M. Pruneanu, *Chemosensors*, 2021, **9**, 146.

67 A. Dey, J. Pradhan, S. Biswas, F. Ahamed Rahimi, K. Biswas and T. K. Maji, *Angew. Chem., Int. Ed.*, 2024, **63**, e202403093.